

El Niño as a Natural Experiment for Studying the Tropical Tropopause Region

A. GETTELMAN, W. J. RANDEL, S. MASSIE, AND F. WU

National Center for Atmospheric Research, Boulder, Colorado

W. G. READ

NASA Jet Propulsion Laboratory, Pasadena, California

J. M. RUSSELL III

Center for Atmospheric Sciences, Hampton University, Hampton, Virginia

(Manuscript received 27 October 2000, in final form 8 February 2001)

ABSTRACT

The interannual variability of the tropical tropopause region between 14 and 18 km is examined using observations of convection, winds, and tropopause temperatures from reanalyses and water vapor from satellites. This variability is compared to a simulation using the Community Climate Model version 3 (CCM3) general circulation model forced by observed sea surface temperatures. A coherent picture of the effect of the El Niño–Southern Oscillation (ENSO) on the tropopause region is presented in the NCEP–NCAR reanalyses and CCM3. ENSO modifies convection in the Tropics, and the temperature and circulation of the tropical tropopause region, in agreement with idealized models of tropical heating. CCM3 reproduces most details of these changes, but not the zonal mean temperature variations present in the analysis fields, which are not related to ENSO. ENSO also forces significant changes in observed and simulated water vapor fields. In the upper troposphere water vapor is at maximum near convection, while in the tropopause region water vapor is at minimum in the regions of convection and surrounding it. Convection, cirrus clouds, temperatures, and transport are all linked to describe the water vapor distribution and highlight the role of transport in the tropopause region.

1. Introduction

The exchange of air across the tropical tropopause region regulates the water vapor content of the upper troposphere and lower stratosphere (Brewer 1949), which is important for the radiative balance of the atmosphere (de F. Forster and Shine 1999; Shindell 2001). Over the last 20 yr, observations indicate rising concentrations of stratospheric water vapor (Michelsen et al. 2000; Oltmans et al. 2000). The causes of this trend can only partially be attributed to the increase in atmospheric methane, which is oxidized to produce water vapor (Oltmans et al. 2000), so that the future direction of these trends is uncertain. Much of this uncertainty stems from a lack of understanding of processes governing water vapor transport from the upper tropical troposphere into the stratosphere. As recently reviewed by SPARC (2000), these processes are thought to be dependent on winds, temperature, convection, and cirrus clouds in the upper tropical troposphere, as well as non-local processes in the stratosphere.

One approach to understanding the important processes around the tropopause is to examine natural variability in the region. Large-scale variability in the tropopause region is dominated by an annual cycle and longer-term interannual variability. In this study we seek to build upon previous analyses of the tropical upper troposphere–lower stratosphere and focus on the differences between phases of the El Niño–Southern Oscillation (ENSO). Using observations and a climate model for comparison, details of ENSO variability are analyzed in convection, winds, tropopause temperatures, and water vapor. From this analysis, we deduce some of the linkages between these fields and processes that control how air enters the stratosphere in the Tropics.

ENSO is the most significant mode of interannual variability of the tropical troposphere. The Southern Oscillation was originally analyzed by Sir Gilbert Walker (e.g., Walker and Bliss 1932) and reviewed by Philander (1990). The ENSO cycle has two distinct phases: a “warm” phase in which a tongue of anomalously warm surface water spreads westward from the eastern Pacific to the date line, and a “cold” phase (sometimes called La Niña) in which there is a broad tongue of anoma-

Corresponding author address: A. Gettelman, National Center for Atmospheric Research, Box 3000, Boulder, CO 80307-3000.
E-mail: andrew@ucar.edu.

lously cold water in this region. These two phases have profoundly different patterns of wind and convection throughout the tropical atmosphere (Philander 1990). These changes also affect upper-tropospheric temperatures (Kiladis et al. 2001; Reid and Gage 1985; Yulaeva and Wallace 1994), as well as upper-tropospheric winds, water vapor, and ozone (Chandra et al. 1998; Newell et al. 1996). The effect of ENSO is a maximum in the boreal (Northern Hemisphere) winter and spring, which is also the time of coldest tropopause temperatures (Highwood and Hoskins 1998) and lowest water vapor concentrations (Holton et al. 1995). Layered on top of a distinct annual cycle in the tropical upper troposphere–lower stratosphere (Holton et al. 1995; Reid and Gage 1981, 1996), ENSO is a natural experiment with two different realizations of the organization of convection and the circulation during its warm and cold phases.

The goal of this work is to analyze ENSO variability in the region of the tropical tropopause using observations and an idealized climate simulation. While much of the description of observed fields has been individually discussed elsewhere, we will review and codify previous analyses into a consistent picture. We will compare the analysis to a climate model that is forced by observed sea surface temperatures (SSTs). The data and analysis techniques used are described in section 2. Patterns of convection are examined in section 3. Tropical circulation patterns are discussed in section 4. Tropopause temperatures are analyzed in section 5, and recently available measurements of water vapor in the upper troposphere and lower stratosphere are discussed in section 6. Throughout we will compare observations to model simulations, and attempt to discuss the coupled nature of these fields. Discussion and conclusions are presented in section 7.

2. Methodology and datasets

Several different analyses are used to examine the interannual variability in deseasonalized fields from observations and models. These analyses include composite or seasonal averages and difference maps, linear regression with indices of interannual variability such as ENSO, and empirical orthogonal function (EOF) analysis. EOF analysis of geophysical fields is discussed by Lorenz (1956). Data considered include outgoing longwave radiation (OLR), wind fields, tropopause temperatures, and water vapor from both satellite data and an atmospheric model.

The tropical tropopause is not a material surface, but rather the slow transition from one stability regime in the troposphere (convective equilibrium) to another (radiative equilibrium) in the stratosphere. As noted by Folkins et al. (1999), ozone observations suggest a slow transition between purely stratospheric and purely tropospheric air in this region. So following Atticks and Robinson (1983) and Highwood and Hoskins (1998), we will speak of the region of interest in the upper

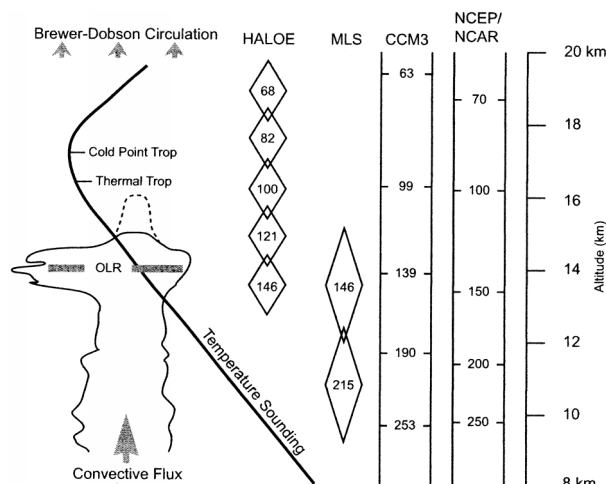


FIG. 1. Schematic representation of data used for the study by pressure level (hPa) with a schematic of temperatures, clouds, and terms used. Altitude scale on right (km).

tropical troposphere as the “tropical tropopause region.” This region is defined as extending from the main convective outflow level at approximately 150 hPa to the temperature minimum (“cold point”) at about 95 hPa.

We will use two definitions of the tropopause: the thermal or lapse rate tropopause, and the cold point tropopause, often located slightly higher. The thermal or lapse rate tropopause is defined according to the World Meteorological Organization as the first point at which the lapse rate drops below $2^{\circ}\text{C km}^{-1}$ in a layer at least 2 km deep. Practically it falls near 100 hPa, well into the tropopause region. We use both the temperature and potential temperature of the lapse rate tropopause as diagnostics. An alternative definition of the tropopause is the cold point tropopause, or the point of minimum temperature in a profile. The temperature and pressure of the cold point is perhaps more useful for estimating stratospheric water vapor [as discussed by Zhou et al. (2001)]. The cold point is often a kilometer or more above the thermal tropopause (Seidel et al. 2001). As discussed by Highwood and Hoskins (1998) it is difficult to calculate the cold point from coarse vertical resolution reanalysis data available at standard pressure levels of 150, 100, 70, and 50 hPa (illustrated schematically in Fig. 1). Calculating the cold point tropopause from such coarse analysis data using a cubic spline interpolation yields a diagnostic surface whose temperature is very close to that of the thermal tropopause, but whose altitude is often a kilometer above (hence its potential temperature is often very different).

Tropopause diagnostics (temperature, pressure, and potential temperature) and wind fields are derived from the National Centers for Environmental Prediction (NCEP) and National Center for Atmospheric Research (NCAR) reanalyses (Kalnay et al. 1996), hereafter the NCEP–NCAR reanalyses. In this study, we focus on

monthly averages derived from observations four times a day. OLR interpolated from satellite brightness temperature data by the National Oceanic and Atmospheric Administration (NOAA) is used as a proxy for the location of convection. NCEP–NCAR reanalysis and NOAA interpolated OLR data are provided by the NOAA–Cooperative Institute for Research in Environmental Sciences (CIRES) Climate Diagnostics Center, Boulder, Colorado (available online at <http://www.cdc.noaa.gov/>). For these analyses we will focus on the period from 1979 to 1999. We have chosen this period mostly because tropopause level data reveal a step change in time series that occurred when assimilation of satellite data into the analysis system began (Randel et al. 2000). This data period yields reasonable length time series for analysis and several ENSO warm and cold events. As discussed by Seidel et al. (2001), the reanalyses system may generate different tropopause characteristics than radiosonde data (due to coarse vertical resolution), but Randel et al. (2000) have shown that the NCEP data has similar variability to radiosondes on the scales of interest here (monthly to interannual).

For comparison with these assimilated observations, OLR, winds, tropopause temperatures, and water vapor fields have been simulated by running the NCAR Community Climate Model version 3 (CCM3), forced by observed SSTs. The climate model is described by Kiehl et al. (1996). The simulation extends from 1950 to 1999, and SSTs are prescribed based on analyzed monthly averaged SST data from NCEP. Analyses from the model are taken from the period 1979–99, which overlaps the satellite period in the NCEP–NCAR reanalyses. Horizontal model resolution is approximately 2.8° latitude and longitude, which is similar to the NCEP–NCAR reanalyses. Vertical resolution of the model is illustrated schematically in Fig. 1.

For comparison of these time series, we have used an ENSO index of SST anomalies (SSTAs) in the tropical eastern Pacific from 5°S to 5°N and 150° to 90°W . This region is known as the Niño-3 region. The results are not sensitive to the particular region chosen (SST anomalies from other regions work just as well). These indices were obtained from the NOAA–CIRES Climate Diagnostics Center.

The study also incorporates observations of water vapor and cirrus cloud extinction. These data come from two instruments on board the *Upper Atmosphere Research Satellite* (UARS). Water vapor observations in the upper troposphere are available from the Microwave Limb Sounder (MLS) on UARS from October 1991 to April 1997. The MLS upper-tropospheric observations are available in the Tropics at 146, 215, 316, and 464 hPa (Read et al. 1995). Version 4.9 data is used in this study. MLS has a vertical resolution of ~ 3 km (see Fig. 1), which is relatively coarse compared to the vertical gradients of water vapor in the tropopause region. MLS water vapor retrievals are considered most accurate at the 215-hPa level (Read et al. 1995) and we focus on

these data here. Water vapor in the tropopause region is also available from the Halogen Occultation Experiment (HALOE), described by Russell et al. (1993) and Harries et al. (1996). We use version 19 data, gridded in a manner described by Randel et al. (2001). HALOE has a vertical field of view of ~ 1.6 km in the tropopause region (illustrated in Fig. 1). The detailed space–time climatology of water vapor in the tropopause region is discussed by Jackson et al. (1998) and Randel et al. (2001), while here we focus on interannual variations associated with ENSO. In addition to water vapor, HALOE measures atmospheric aerosol. Using the methodology of Massie et al. (2000), large aerosol extinctions measured by HALOE indicate the presence of cirrus clouds (water ice), which at the altitudes and extinctions reported are largely “subvisible.”

As noted by Harries et al. (1996), the HALOE instrument is observing at the low end of its altitude range in the lowest stratosphere, and uncertainties in individual measurements are high. Because it is a solar occultation instrument, HALOE may only sample a particular latitude and longitude region in the Tropics a few times a month. HALOE is also subject to a bias because it cannot see through thick clouds. The MLS upper-tropospheric channel has a detection limit of 10 parts per million by volume (ppmv), which limits its observations to the troposphere. In addition, temporal sampling from the MLS instrument is incomplete, particularly during the last few years of the instrumental record. We will thus limit ourselves to fairly coarse monthly averages and mostly qualitative conclusions from these data.

3. Location of convection

The contrast between the recent 1997–98 El Niño (ENSO warm event) and the 1998–99 La Niña (ENSO cold event) illustrates the changes in the tropical atmosphere. Changes in SSTs force significant changes in convective activity. In this analysis, NOAA interpolated OLR is used as a proxy for the location of convective activity. Figure 2 illustrates the seasonal mean distribution of OLR for these two periods, with their difference. During ENSO [December–February (DJF) 1998] convection (low OLR) moves into the central and eastern Pacific (Fig. 2a), while during the La Niña cold event (DJF 1999) it is concentrated over the maritime continent and the western Pacific south of the equator (Fig. 2b). Throughout this work, the DJF season will be referred to by the later year in many of the figures for clarity. The maximum decrease in OLR (increasing convection) during ENSO warm periods extends from the date line eastward. Similar patterns have previously been illustrated for other ENSO events or a composite of events by Philander (1990), Deser and Wallace (1990), Yulaeva and Wallace (1994), and Kiladis et al. (2001) (among others).

The ENSO variability can be isolated by performing

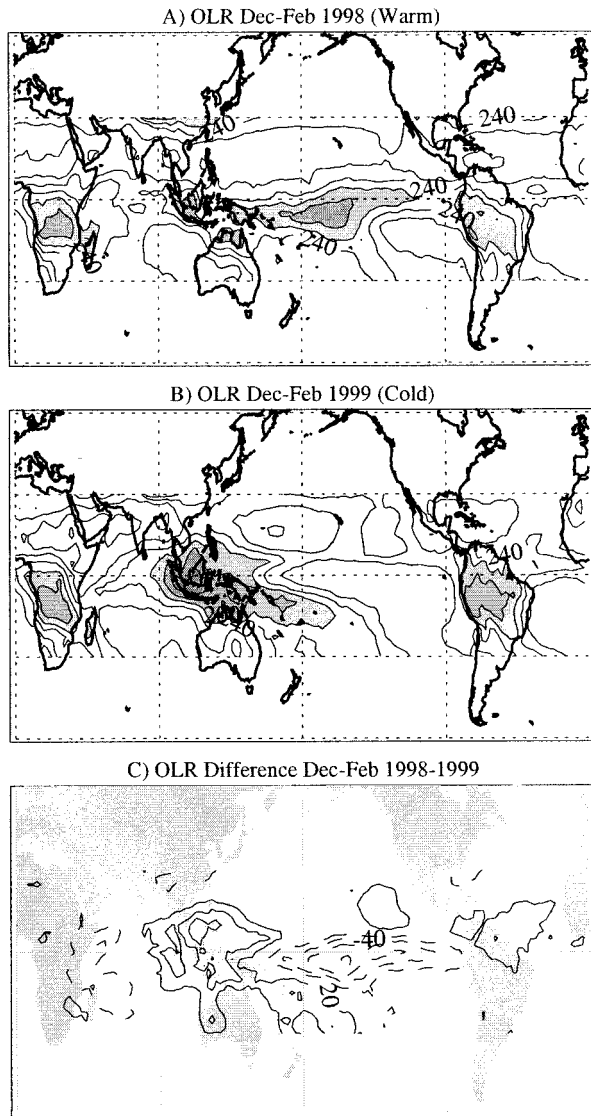


FIG. 2. Seasonal (DJF) mean OLR (W m^{-2}) from 30°S to 30°N for (a) 1997–98 (ENSO warm), (b) 1998–99 (ENSO cold), and (c) the difference between them. Contour interval of 20 W m^{-2} with levels below 220 W m^{-2} shaded in (a) and (b). Contour interval of 15 W m^{-2} in (c).

an EOF analysis of deseasonalized (annual cycle removed for each month) monthly mean OLR (Fig. 3a). The principal component (PC) of the leading mode of interannual variability of convection (Fig. 3c solid line) is strongly correlated with SST anomalies in the Niño-3 region (Fig. 3c dotted line), with a linear correlation coefficient 0.84. The EOF pattern is similar to the difference pattern in Fig. 2c or to a regression of Niño-3 on the OLR (Kiladis et al. 2001). In this and other EOF analyses, the mode is scaled to physical units (W m^{-2} in this case) associated with one standard deviation (σ) of the PC, and $\pm 1\sigma$ of the PC is marked with dotted lines on the time series in Fig. 3c. Thus the strong ENSO

events of 1997–98 and 1982–83 in this mode are associated with nearly three times the 1σ change in OLR ($\sim 45 \text{ W m}^{-2}$), slightly less than the maximum in Fig. 2c. This pattern explains 18% of the variance of the data. There is a second statistically significant EOF in the analysis of OLR (not shown), which explains a further 8% of the variance, and also maps strongly onto the central and western Pacific. This mode is in quadrature with the first EOF, maximizing about 6–9 months after the maximum SST anomalies of the Niño-3 ENSO index (lag correlation at 8 months is 0.35). The second mode is also present in the analysis of OLR in the CCM, and corresponds to a longitudinal shifting of the OLR patterns during an ENSO cycle (rather than just a seesaw variation). Its properties are similar to a second ENSO mode (the “Trans-Niño Index”), described by Trenberth and Stepaniak (2001), which captures the evolution of an ENSO event before and after its peak. However, the variance associated with this second mode is not high enough to map strongly upon the other fields considered in this study, and is not discussed further here.

Conducting the EOF analysis using only certain months allows some discrimination of the relationship between these modes and the annual cycle. Analyzing only 6 months of the year in the analysis reveals that the mode in Fig. 3 explains more of the variance in November–April OLR (23%) than it does from May–October (16%), with approximately the same correlation with Niño-3 SSTAs (0.87 and 0.89, respectively). This is consistent with the largest warm anomalies due to ENSO occurring in the early months of the calendar year (Philander 1990).

An identical EOF analysis was performed on the monthly mean OLR derived from a run of CCM3 forced with observed SSTs. For the period 1979–99, the EOF analysis of OLR from the CCM3 simulations (Fig. 3b), which explains 16% of the variance, yields a mode very similar to that of the first EOF of observed OLR (Fig. 3a). The PC time series in the simulation is very similar to that of the observations (Fig. 3c), correlated with the Niño-3 index at 0.87 and the NOAA OLR PC at 0.86. The patterns in the observations (Fig. 3a) and in CCM3 (Fig. 3b) are both broadly similar to the difference pattern in Fig. 2c. However, in the model, the maximum increase in OLR associated with El Niño (negative ENSO anomalies) in the western Pacific is located farther east than in the observed OLR, and the anomalies over the Maritime Continent are much smaller at the equator. While the first EOF of observed OLR (Fig. 3a) has a strong zonally oriented dipole, the tripolar structure in the first EOF of CCM3 OLR (Fig. 3a) is more meridional.

This comparison demonstrates that the ENSO changes in tropical convection are well characterized in the forced CCM3 simulation. ENSO is the dominant mode of interannual variability of monthly mean convection in both observations and the model. The effect of ENSO is particularly strong during the recent ENSO warm and

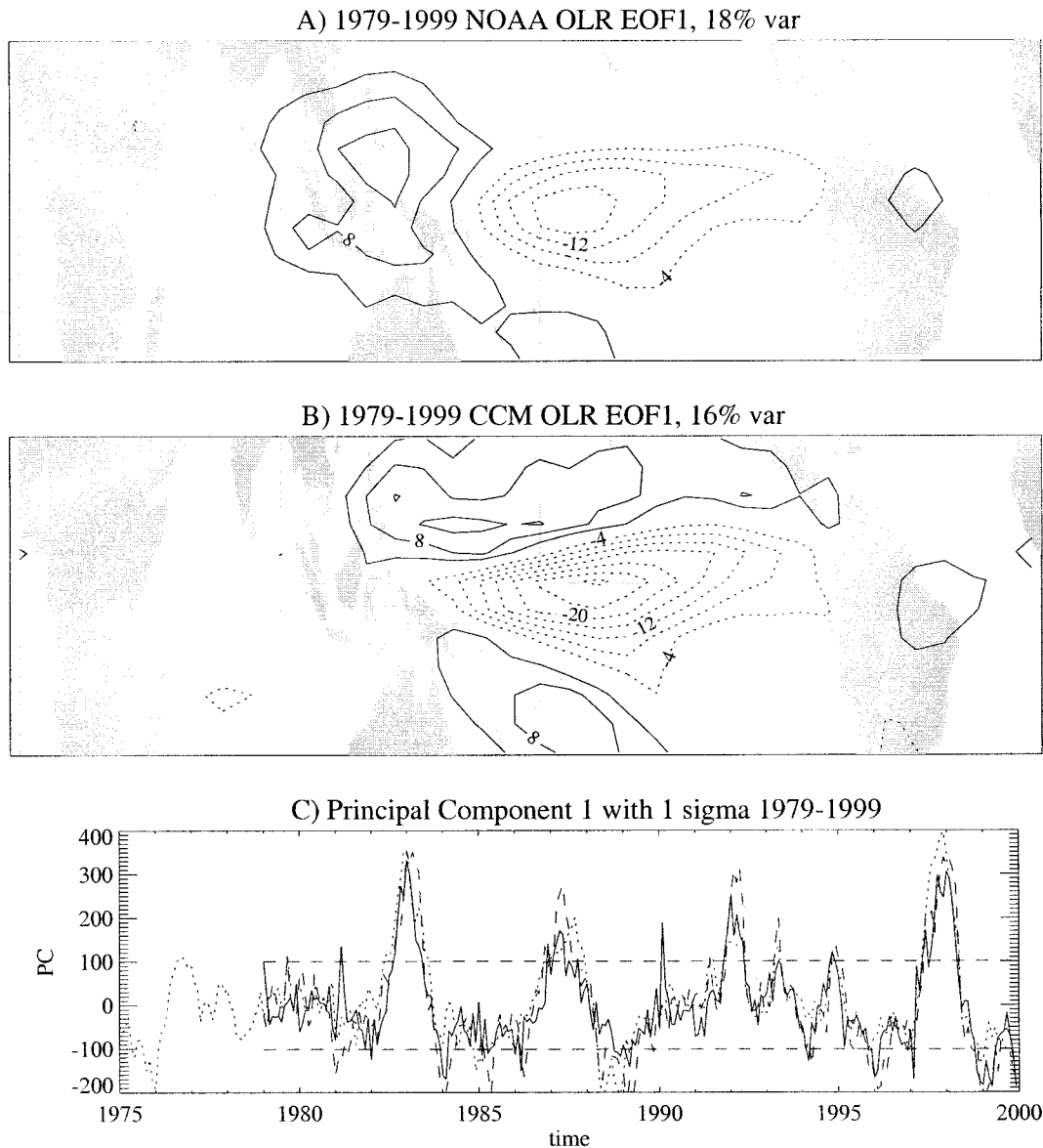


FIG. 3. (a) Leading EOF mode of deseasonalized OLR from monthly NOAA observations. Analyzed from 1979 to 1999 in units of W m^{-2} per std dev of principal component time series. (b) Leading mode for 1979-99 OLR from the CCM3 run forced by observed SSTs. (c) Solid line: Principal component (PC) time series of the EOF in (a). Dashed line: PC of the model EOF in (b). Dotted line: scaled Niño-3 SSTA. Dashed horizontal lines represent $\pm 1\sigma$ of all three time series.

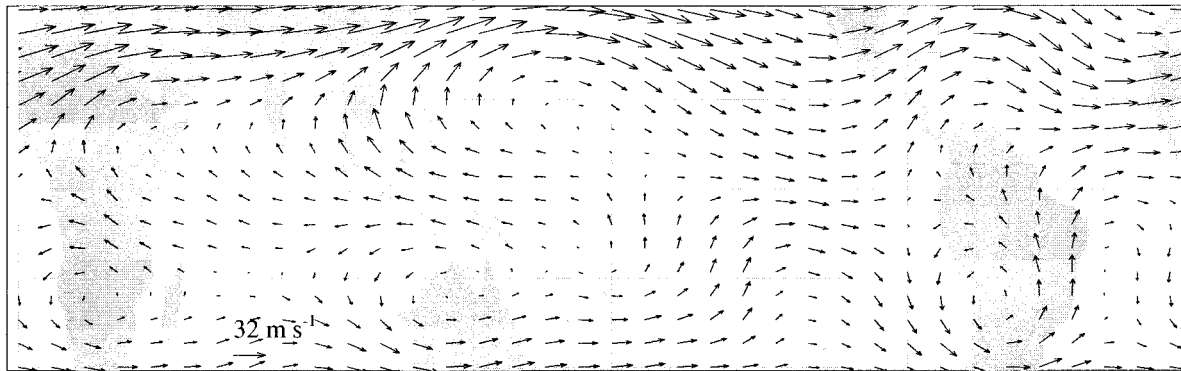
cold event from 1997-99. In the next section we look at how these changes affect the wind patterns in the upper troposphere.

4. Circulation patterns

Changes in the pattern of convection have a significant impact on the tropical circulation. The average upper-level winds for January at 150 hPa and the associated divergence pattern are illustrated in Fig. 4. Two anticyclonic wind gyres are present in the western Pacific, with eastward flow over the eastern Pacific and

westward flow over the Indian Ocean. The Northern Hemisphere winter jet stream is visible at the top of Fig. 4a. The divergence pattern (Fig. 4b) is marked by divergence at upper levels (indicating rising motion) over the Indian Ocean and Maritime Continent as well as over tropical Africa and South America. Convergence (sinking motion at upper levels) is found over the eastern Pacific and Atlantic Oceans. Note the resemblance of the divergence pattern to the distribution of OLR in Fig. 2, and particularly during an ENSO cold event in Fig. 2b. This flow represents the average state of the Walker circulation (Bjerknes 1969) in January.

A) Jan Average Monthly Mean 150 hPa Wind



B) Divergence

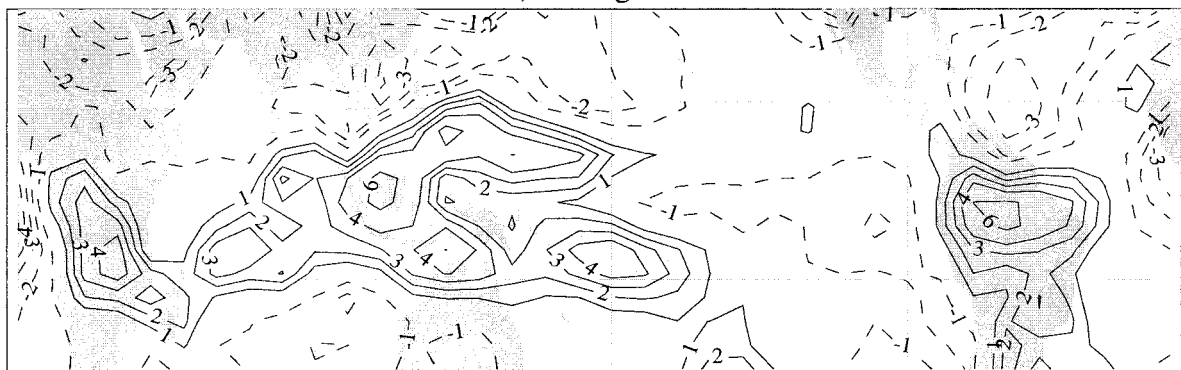


FIG. 4. (a) Average Jan NCEP–NCAR reanalysis (1979–99) monthly vector wind at 150 hPa. (b) Divergence of (a) in units of 10^{-6} s^{-1} , contour interval of $1 \times 10^{-6} \text{ s}^{-1}$.

The shift of convection into the central and eastern Pacific during ENSO warm events modifies the tropical Walker cell circulation significantly (Gage and Reid 1987; Oort and Yienger 1996; Webster 1983). During ENSO warm events the downward branch of the Walker circulation (normally over the eastern Pacific) shifts over the Maritime Continent, resulting in drought conditions over Indonesia [see diagram in Webster (1983) and Gage and Reid (1987)]. It also strengthens the meridional Hadley circulation (Oort and Yienger 1996). Yulaeva and Wallace (1994) attribute this enhanced meridional flow to a dynamical balance for the increased baroclinicity in the subtropics. The enhanced Hadley circulation is visible in composites of ENSO warm events in the meridional wind field in the tropopause region (150–70 hPa) in the NCEP–NCAR reanalysis data (not shown). The intensification extends upward to the 70-hPa level.

The changing Walker circulation during ENSO can be illustrated by regressing the vector wind on an ENSO index (Niño-3), as illustrated in Fig. 5 at 150 hPa. An anticyclonic anomaly is present in both hemispheres in the eastern Pacific, maximizing at over 5 m s^{-1} . Easterlies are enhanced in this region at the equator, while westerly winds are enhanced throughout the rest of the Tropics. This pattern results in a pattern of divergence

and convergence anomalies (Fig. 5b) characterized by enhanced convergence at upper levels during ENSO warm events over Indonesia and the western Pacific, and enhanced divergence at the same time over the central and eastern Pacific. The enhanced divergence is consistent with the convective patterns shown in Figs. 2 and 3: stronger convection in the central and eastern Pacific during ENSO warm events and suppressed convection (convergence at upper levels) in the western Pacific. The regression pattern during strong ENSO events ($3 \times \sigma$) is of sufficient magnitude (compared to Fig. 4b) to change the regions of upward and downward motion.

A similar analysis can be performed on wind fields from the CCM forced by observed tropical SSTs. Figure 6 illustrates a regression similar to that in Fig. 5 but for the 139-hPa level in the model. The patterns in Figs. 5a and 6a are strikingly similar, with anticyclonic anomalies located within 5° of latitude and longitude as those in the analyses. The major difference between the model and the analyses is that the model regression has weaker westerly anomalies over the maritime continent, which may be related to the differences in the convective response over that region (Figs. 3a and 3b). The divergence patterns both feature strong divergence just west of the axis of the anticyclones, and divergence all the

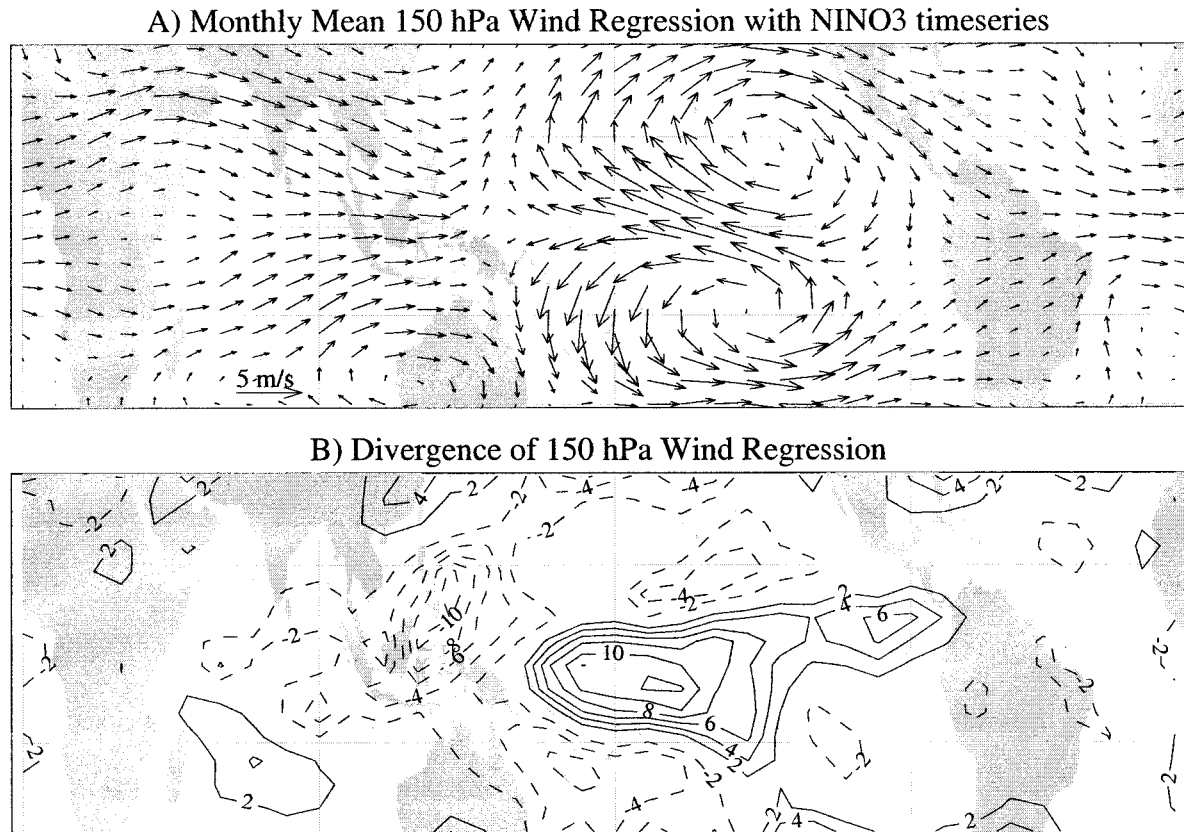


FIG. 5. (a) Regression of NCEP–NCAR reanalysis (1979–99) monthly vector wind on Niño-3 (see text) SSTA time series. (b) Divergence of (a) in units of 10^{-7} s^{-1} , contour interval of $2 \times 10^{-7} \text{ s}^{-1}$.

way to the coast of South America and slightly north of the equator. This pattern tends to reverse the traditional zonal Walker cell circulation in the Pacific. The divergence patterns in Figs. 5b and 6b are consistent with changes in the upward and downward motion diagnosed from pressure vertical velocities in the CCM simulation.

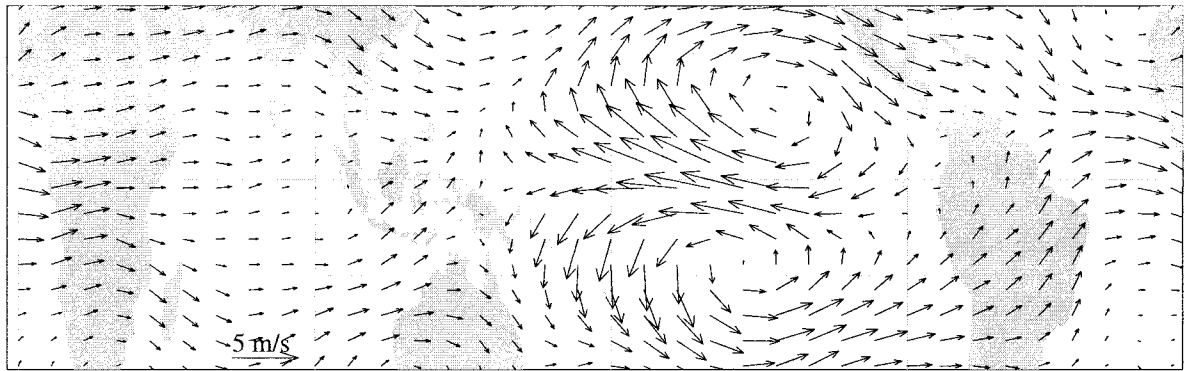
Before attempting to explain the patterns in the upper troposphere in Figs. 5 and 6, we will briefly consider their vertical extent. Figure 7 illustrates that the patterns in Figs. 5b and 6b have maximum magnitudes (as measured by the maximum divergence and convergence anomalies in the Tropics) at 150 hPa and fall off in magnitude above and below. Magnitudes then increase again in the lower troposphere (though not surprisingly with opposite polarity in the geographic locations of convergence and divergence). The maxima at 150 hPa are consistent with the level of main convective outflow (the altitude reached by most deep convection) over much of the tropical Pacific.

These anticyclonic circulation anomalies located off the equator at the longitude of enhanced convection in the central Pacific have also been noted by Yulaeva and Wallace (1994). These observed anomalies are consistent with Rossby gyres and Kelvin wave responses to

an idealized heating on the equator both in linear models (Gill 1980) and in multilevel baroclinic models (Highwood and Hoskins 1998). It is also consistent with the stochastic forcing in the baroclinic model of Salby and Garcia (1987). The position of the gyres is to the east of the maximum convective anomaly (Fig. 3a) or the divergence anomaly (Fig. 5b), while the classic “Gill model” solution for a tropically induced circulation would predict Kelvin wave propagation eastward, planetary wave propagation westward, and circulation anomalies off the equator to the west of the heating center (Gill 1980). The use of a model allows the total heating field to be examined (shortwave + longwave + latent heat). A regression of this total heating field from CCM3 on the Niño-3 index (Fig. 8) indicates that the change in total tropospheric column-integrated latent heating associated with ENSO has a broad maximum that extends along the equator out to nearly 135°W , and that ENSO causes heating anomalies that extend all the way to the coast of South America, and are not just confined to the central Pacific. The response over the maritime continent is not as strong (which may be the reason for the differences noted between the simulation and observations).

The response to the model heating described here is

A) 139mb CCM Wind Regression with NINO3 timeseries



B) Divergence of 139mb CCM Wind Regression

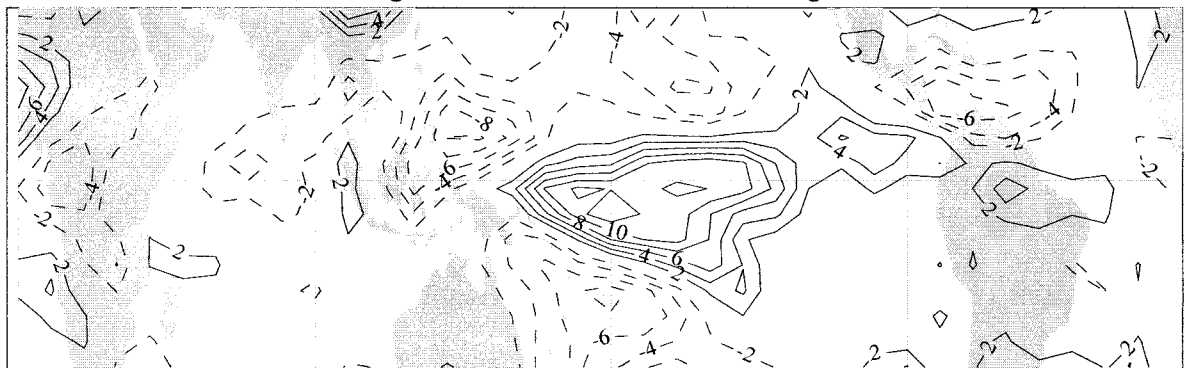


FIG. 6. (a) Regression of CCM3 (1979–99) monthly vector wind at 139 hPa on El Niño-3 SSTA time series. (b) Divergence of (a) in units of 10^{-7} s^{-1} , contour interval of $2 \times 10^{-7} \text{ s}^{-1}$.

different from the analysis of the 1982–83 ENSO warm event by Sardeshmukh and Hoskins (1985), who found heating anomalies only in the central Pacific, west of the circulation anomalies. Sardeshmukh and Hoskins (1985) conclude that nonlinearities are important, while

in the CCM simulation it appears as if the circulation anomalies in the Pacific forced by the total heating anomalies are well described by a linear model. The model heating is also confined narrowly to the equator, which may be part of the reason for the extended zonal character of the CCM OLR EOF pattern in Fig. 3 and the differences with observations over the maritime continent.

Thus the upper-tropospheric circulation responds to changes in the integrated tropospheric heating during ENSO (primarily latent heat release in the lower levels of the atmosphere), consistent with idealized models of tropical heating. This heating is similar to the OLR patterns. These circulation and heating changes are likely to have significant effects on tropopause temperatures, which are analyzed in the next section.

5. Tropopause temperature

Changes in convection and circulation patterns as a result of changes in SST have been shown to have an effect on the tropopause temperature (Reid and Gage 1985) and the gradients of potential temperature (Gage and Reid 1987). These properties can be analyzed at several levels in the tropopause region. Here we choose

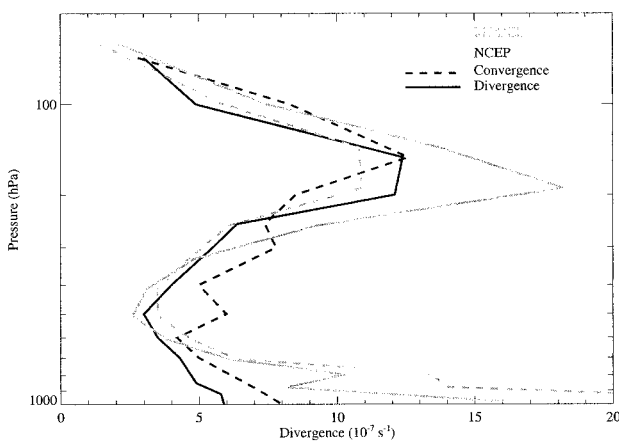


FIG. 7. Maximum divergence (solid line) and convergence (dashed line) of a regression of 1979–99 monthly vector wind on Niño-3 (see text) SSTA time series from NCEP–NCAR reanalyses (black lines) and CCM3 (gray lines). Units of 10^{-7} s^{-1} .

Vert Integrated (117–1000mb) Regression with NINO3 timeseries

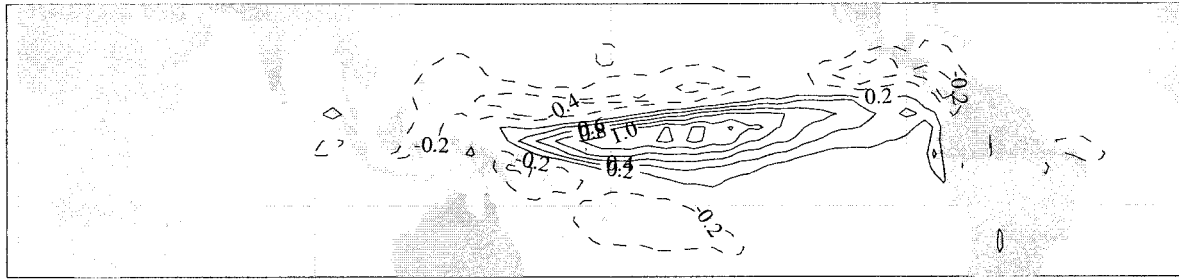


FIG. 8. Regression of 1979–99 monthly tropospheric integrated total heating from CCM3 on El Niño-3 (see text) SSTA time series from NCEP–NCAR reanalyses. Units of K day^{-1} .

two levels: the lapse rate tropopause and the slightly higher cold point tropopause. A detailed discussion of the climatological characteristics of the lapse rate and cold point tropopauses can be found in Seidel et al. (2001).

As discussed by Randel et al. (2000) and Seidel et al. (2001), there are significant interannual variations in zonally averaged tropical tropopause temperatures. Figure 9 displays the departures from the long-term monthly average over the Tropics (25°S – 25°N) for both the NCEP reanalysis thermal tropopause and the CCM thermal tropopause. A plot of the cold point tropopause temperature anomalies would look virtually the same. The solid line has previously been generated for the NCEP–NCAR reanalysis tropopause by Randel et al. (2000), who note that while the data accurately reflect the range of variability in an equivalent tropopause temperature time series calculated from averaged radiosonde data, there are significant differences in detail (particularly for the years 1986–92). The correlation of the NCEP anomalies with the Niño-3 SSTA index is -0.27 , while for the model anomalies, the correlation is 0.31 . Neither is significantly different from zero at the 95% level using a Student's *t*-test with 21 degrees of freedom (one for each year). Thus, ENSO has a small

influence on the zonal mean tropopause temperature in either observed or modeled data. Furthermore, the NCEP analyses have a standard deviation (σ) of 0.81°C , nearly three times the model σ of 0.32°C . The reduced variability in the simulation is not surprising. The model does not resolve the stratospheric quasi-biennial oscillation (QBO), and it does not represent the volcanic eruptions of El Chichón (1982) and Mount Pinatubo (1991). These events are significant forcings on tropopause temperatures in the NCEP analyses, as discussed in detail by Randel et al. (2000).

To analyze the ENSO influence on the tropical tropopause temperature, we remove this zonal mean signal from the data (as performed earlier for the OLR analyses in section 3). The resulting leading EOF patterns are illustrated in Fig. 10 for the NCEP–NCAR reanalysis tropopause (Fig. 10a) and for the CCM3 tropopause (Fig. 10b). The principle components (PC) of the first tropopause EOF shown in Fig. 10 are correlated with the Niño-3 SSTA index at a level of 0.74 (NCEP) and 0.77 (CCM3). Both feature strong negative dumbbell shaped maxima associated with positive Niño-3 anomalies, maximizing at about 20° off of the equator. Referring back to the ENSO SSTA time series in Fig. 3, the large ENSO events of 1982–3 and 1997–8 corre-

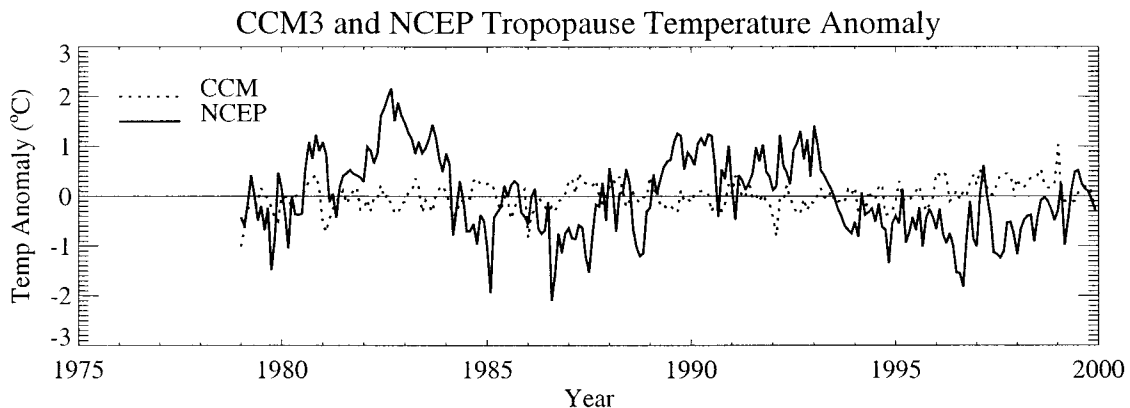


FIG. 9. Tropical average (25°S – 25°N , all longitudes) thermal tropopause temperature anomaly for NCEP–NCAR reanalyses (thick solid line) and CCM3 tropopause (dotted line). Zero line marked as a thin solid line.

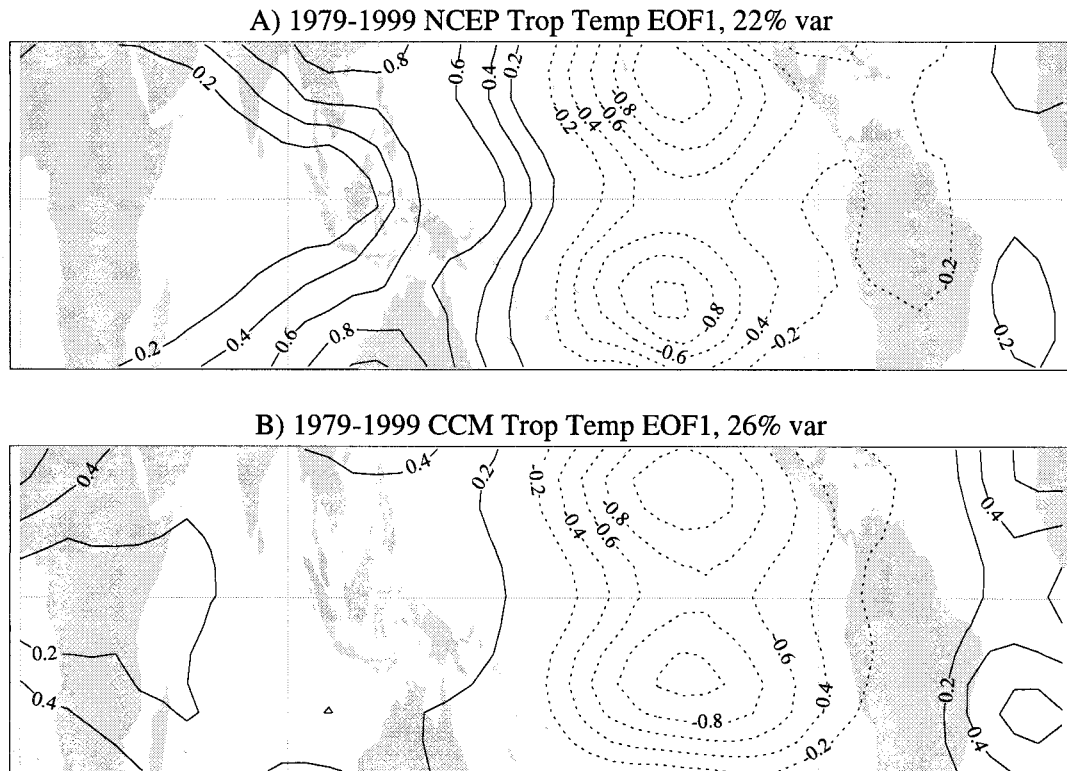


FIG. 10. First EOF of thermal tropopause temperature anomalies 1979–99, scaled to units of $^{\circ}\text{C}$ per std dev of the PC. (a) NCEP–NCAR reanalysis tropopause. (b) CCM3 tropopause.

respond to three to four times the standard deviation of the time series, implying a 3° – 4° cooling at the tropopause in this region, as shown in Tahiti and Darwin tropopause statistics from radiosondes in Randel et al. (2000). These dumbbell-shaped maxima are very similar between the analyses and the model. There are oppositely signed maxima in both the model and the analyses over the Atlantic, though those in the CCM are stronger. Over the Indian Ocean the CCM tropopause shows less structure than that in the reanalyses, likely due to the difference in convection and winds between the simulation and observations in this region. These EOFs are quite similar to each other in the Pacific.

These ENSO patterns are fairly robust and have been seen in similar analyses by Randel et al. (2000) and Kiladis et al. (2001). The dumbbell pattern was also observed by Zhou et al. (2001) in ENSO warm and cold composites of the cold point tropopause temperature, and in tropospheric and lower-stratospheric temperatures by Yulaeva and Wallace (1994).

The dumbbell pattern in the central Pacific in Fig. 10 is collocated in longitude with the anticyclones in Fig. 5. However, the pattern in Fig. 10 is broader in latitude than in Fig. 5. In the simple linear model of Gill (1980), and the baroclinic model of Highwood and Hoskins (1998), the temperature anomalies at the tropopause are consistent with an equatorial heating in the troposphere, located to the east of the temperature maxima along the

equator, in a location very similar to the heating associated with ENSO in the CCM illustrated in Fig. 8. Beyond the Pacific basin, the attribution of forcing to the anomalies is complicated. The Atlantic maxima of opposite sign may be related to enhanced heating over South America during the cold phase of ENSO. Such a response is consistent with the small OLR anomalies over South America in Fig. 3 and the enhanced (negative) divergence pattern during La Niña over Africa in the CCM (Fig. 6). However, the anomalies in tropopause temperature over the Atlantic may also be a barotropic response to heating in the central and eastern Pacific (Sardeshmukh and Hoskins 1985, 1988). Over the Indian Ocean, the behavior of ENSO is likely complexly coupled with the south Asian monsoon (Webster et al. 1998).

In the EOF analysis of the NCEP tropopause temperature, there is a second significant EOF, which explains 15% of the variance and is highly correlated with indices of the stratospheric QBO, an oscillation of the zonal wind direction in the stratosphere. Further analysis of this signal at the tropopause level is discussed by Randel et al. (2000) and Giorgetta and Bengtsson (1999). The CCM3 does not have a QBO in the stratosphere, so this mode of variability is absent in CCM3 tropopause temperature.

The relationship between the tropopause and the troposphere below can also be analyzed using the potential

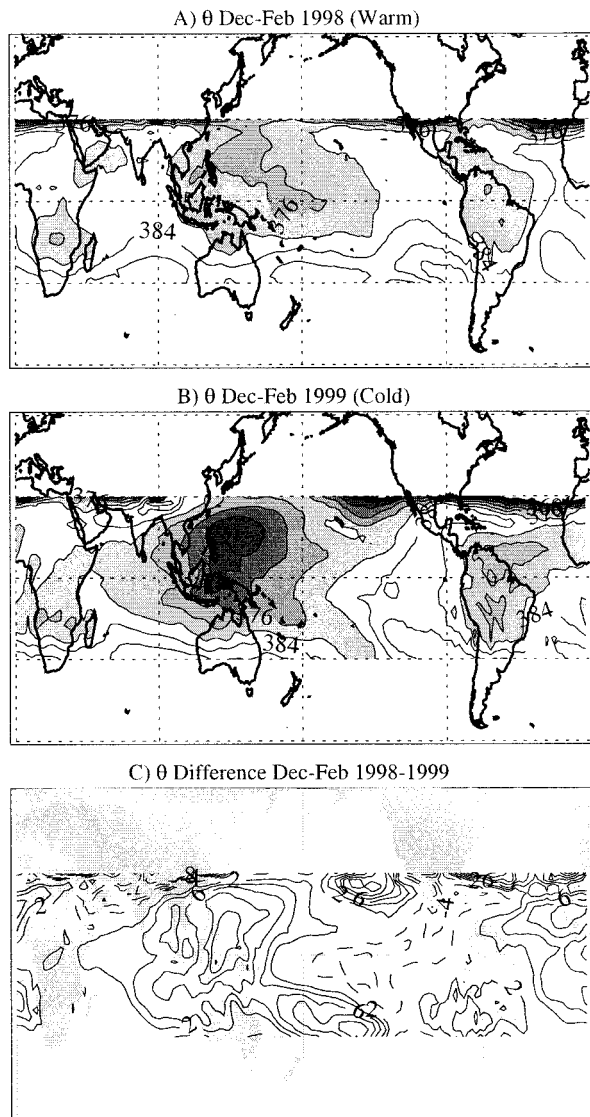


FIG. 11. Seasonal (DJF) mean potential temperature (θ) on the tropopause from 30°S to 30°N for (a) the ENSO “warm” event of 1997–98, (b) the ENSO “cold” event of 1998–99, and (c) the difference between them. Contour interval of 4 K with levels below 380 K shaded in (a) and (b). Contour interval of 2 K in (c).

temperature of the tropopause. The potential temperature of the analyzed tropopause (either using the thermal definition or the cold point) is a convolution of the tropopause pressure and temperature [potential temperature or $\theta \equiv T(p_0/p)^{R/C_p}$]. Theta is not changed by adiabatic motion and thus is a good measure of how much heating (whether latent, sensible, or radiative) a parcel has experienced, or how much heating is necessary to lift a parcel to some level in the stratosphere. The potential temperature (θ) of the analyzed tropopause has a slightly different morphology than the temperature of this surface because it is convolved with pressure changes on the tropopause. At the equator, there are zonal

variations of up to 20 K (at 100 hPa 1 K \approx 0.5°C) in tropopause θ during ENSO cold events (Fig. 11b). During ENSO warm events, consistent with Fig. 10, the coldest regions in the western Pacific warm, and the central and eastern Pacific cools, reducing zonal variations to 10 K (Fig. 11a).

The difference map in Figure 11c, is similar to the pattern generated from an EOF analysis of the tropopause potential temperature anomalies (Fig. 12). The linear correlation coefficient of this mode’s principle component with the Niño-3 SSTA index is 0.64. A similar spatial pattern is also present in the first mode of an EOF analysis of the CCM3 tropopause potential temperature anomalies (not shown). The spatial distribution of this pattern isolated either as an EOF mode (Fig. 12) or as a difference map (Fig. 11c), does not at first glance resemble the temperature anomaly dipole pattern of Fig. 10. Rather it is similar to the OLR patterns in Figs. 2 and 3. This makes logical sense, because the circulation and temperature anomalies away from the direct heating field are approximately balanced with pressure anomalies [not shown here—see, e.g., Kiladis et al. (2001)], so that the potential temperature is not changed. Because θ is only changed by diabatic processes, its variability is most similar to that of the tropospheric heating; note the similarity between the EOF patterns of θ (Fig. 12) and OLR (Fig. 3). Similar results were obtained in a baroclinic model by Highwood and Hoskins (1998), where an equatorial heating anomaly created anticyclonic circulation and associated temperature anomalies to the west, but the potential temperature response was localized above the heating.

In summary, zonal mean tropopause temperature anomalies are distinctly different between the observations and CCM3. We conclude that the zonal mean variability in observations is not a result of ENSO. Beyond this zonal mean signal, ENSO is the dominant mode of interannual variability of the tropopause temperature and potential temperature in both observations and a model. The response of these fields to ENSO is consistent with the wind patterns and a response to changes in the tropospheric heating. The variability of potential temperature (Fig. 12) resembles the shape of the OLR (Fig. 3) or mean tropospheric heating (Fig. 8) patterns. The CCM3 simulation of the dynamics and thermodynamics of the tropopause region does a remarkably good job of simulating changes in the tropical tropopause that occur as a result of ENSO (despite different mean anomalies). Given this basis, we will now move on to examine water vapor fields in the tropopause region.

6. Water vapor and cirrus cloud distributions

Water vapor in the upper troposphere and lower stratosphere is governed by a variety of processes [see chapter 3 of SPARC (2000) for a review], but because of limited observations with widely varying spatial and

1979-1999 NCEP Trop Theta EOF1, 14% var

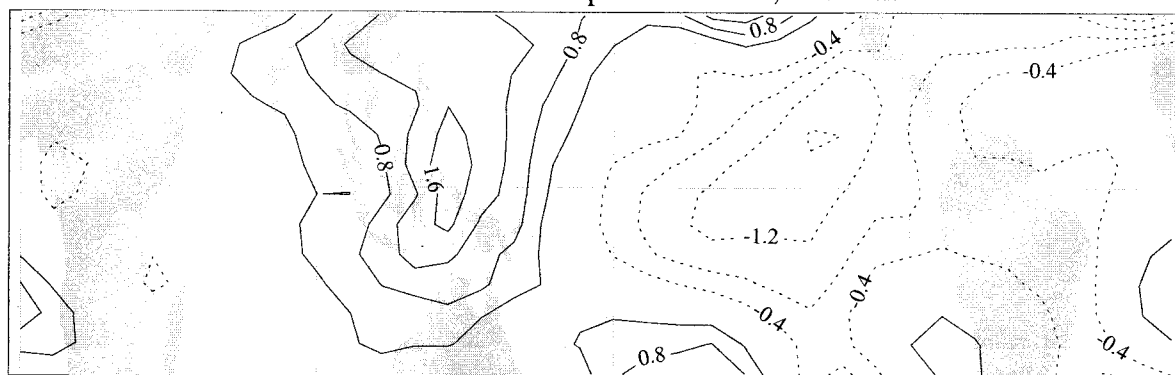


FIG. 12. First EOF of NCEP-NCAR reanalysis tropopause potential temperature anomalies, scaled to units of K per std dev of the PC.

temporal coverage in the Tropics, analysis of interannual variations has been difficult. Here we analyze satellite observations of upper-tropospheric–lower-stratospheric water vapor and cirrus clouds, available across one or several ENSO cycles. Because ENSO has its largest impact on the upper troposphere in boreal winter, and because this is the period of coldest tropopause temperatures and lowest stratospheric water vapor (Mote et al. 1996; Reid and Gage 1981), the analyses will be focused on this season. Kiladis et al. (2001) note that the tropopause response to ENSO is approximately linear (composites of different years look as expected from longer-term regressions). The similarities between composites of the recent 1997–99 ENSO warm and cold event (Fig. 2 for OLR and Fig. 11 for tropopause θ) and their longer term EOFs (Fig. 3 for OLR and Fig. 12 for tropopause θ) yield the same result. This provides a basis for analyzing water vapor in the tropopause region during these different events, even if only a few years are available.

Upper-tropospheric humidity from MLS is available from several years in the early 1990s. In the tropopause region the most relevant levels are at 215 and 147 hPa, with the highest quality observations available at 215 hPa. Seasonally averaged specific humidities (water vapor mixing ratio) at 215 hPa during ENSO warm and ENSO cold years, and their differences, are presented in Fig. 13. Unfortunately, MLS did not provide observations beyond 1997, so a composite of two weaker warm events (1991–92 and 1992–93) and cold events (1995–96 and 1996–97) is used. At 215 hPa, there is a clear shift in the water vapor maximum into the central Pacific during the ENSO warm phase (Fig. 13a) from the western Pacific during the ENSO cold phase (Fig. 13b). High water vapor is also found over South America and Africa just south of the equator during both periods. Warm periods are 50% wetter in the central and eastern equatorial Pacific, and cold periods are significantly wetter near the Philippines in the western Pacific. This is consistent with the analysis of a single ENSO event by Newell et al. (1996) and Chandra et al. (1998).

There is also evidence of significant moistening during ENSO warm events over the Indian Ocean. At 147 hPa (not shown), the picture is not as clear and the percent differences are not as large. The patterns in Fig. 13 resemble the OLR patterns during ENSO warm and cold phases in Fig. 2; that is, the humidity patterns follow the convection. The difference pattern in upper-tropospheric water vapor between these years (Fig. 13c) looks very much like the composite difference pattern in OLR (Fig. 2c) or the EOF pattern in OLR associated with ENSO (Fig. 3a). As noted by Newell et al. (1996), Chandra et al. (1998), and McCormack et al. (2000), upper-tropospheric observations of water vapor show a strong correlation with convective activity, and these changes are naturally linked with changes in convection during the ENSO cycle.

Water vapor is an important trace species in the CCM3 climate model as well. Maps of water vapor mixing ratio (Q) at 190 hPa are illustrated in Fig. 14 for the same periods as the analysis from MLS observations in Fig. 13. As in MLS observations in Fig. 13, the model has a broad maximum in water vapor in the central Pacific and Indian Ocean during ENSO warm events (Fig. 14a), and the maximum is concentrated in the western Pacific during La Niña (Fig. 14b). Note the absolute values of the model at a single pressure level are only about half the MLS values, which are representative of a thick layer in the upper troposphere. However, the relative changes in the model are $\sim 25\%$ – 50% , very similar to the changes in the MLS data. The difference map (Fig. 14c) agrees qualitatively with the changes observed in MLS water vapor (Fig. 13c).

The HALOE instrument provides a retrieval of water vapor in the stratosphere, above the altitude of the MLS measurements (Fig. 1). The vertical resolution (~ 2 km) is higher than the 3-km vertical resolution of the MLS data. It is also higher than the ~ 3 -km resolution of the CCM simulation or the NCEP-NCAR reanalyses in the tropopause region. We will show HALOE water vapor data averaged over a season at two levels, 100 and 82 hPa, near the top of the tropopause region. While some

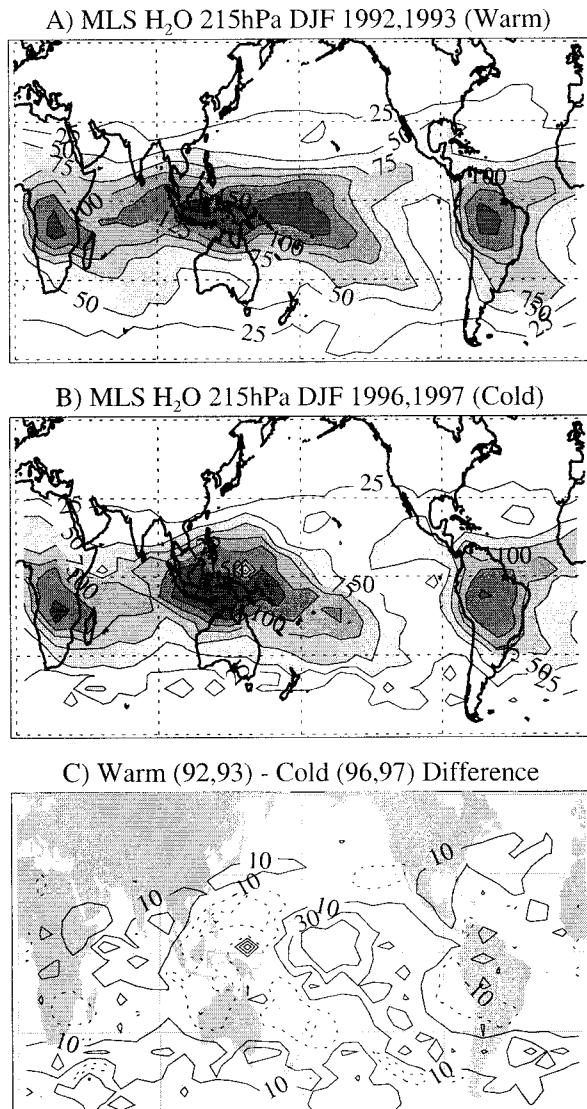


FIG. 13. Seasonal composites of MLS upper-tropospheric humidity (UTH) in parts per million by volume (ppmv) during ENSO warm and ENSO cold events. Composites of monthly mean UTH for four DJF periods: (a) ENSO cold events (1995–96 and 1996–97), (b) ENSO warm events (1991–92 and 1992–93), and (c) Difference between the two (in ppmv). Contour intervals of 25 ppmv for (a) and (b). Levels greater than 50 ppmv shaded. Contour intervals at ± 10 , 30, and 50 ppmv in (c).

quantitative averages are reported, these should be evaluated with caution. Figure 15a illustrates the seasonal distribution of HALOE water vapor at 100 hPa for December–February 1997–98 during a strong ENSO warm event. Water vapor is a minimum (2.9 ppmv) over the western Pacific north and south of the equator and has maxima over the Indian Ocean and tropical South America. The average water vapor mixing ratio in this panel over $\pm 24^\circ$ latitude is 3.7 ppmv. During the 1998–99 ENSO cold event (Fig. 15b), water vapor is a minimum (2.3 ppmv) well north of the equator near the Philip-

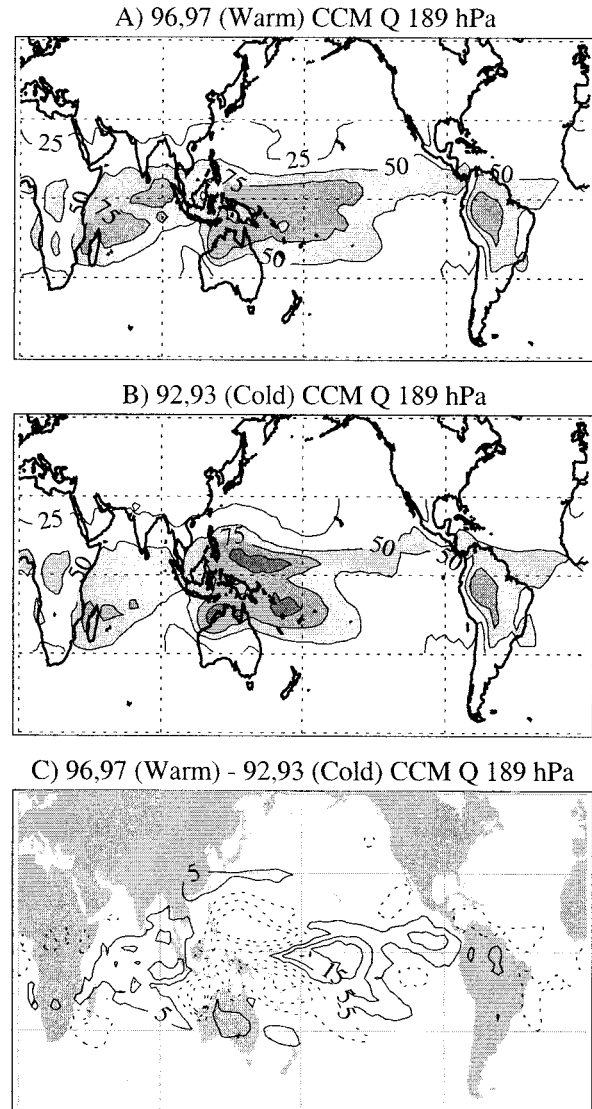


FIG. 14. Seasonal composites of CCM water vapor mixing ratio (Q ; ppmv) at 190 hPa during ENSO warm and ENSO cold events. Composites of monthly mean UTH for four DJF periods: (a) ENSO cold events (1995–96 and 1996–97), (b) ENSO warm events (1991–92 and 1992–93), and (c) difference between the two (ppmv). Contour intervals of 25 ppmv for (a) and (b). Levels greater than 50 ppmv shaded. Contour intervals at ± 5 , 15, and 25 ppmv in (c).

ines, and the minimum extends from the date line west to the Greenwich meridian. Water vapor maxima are located over South America and over the maritime continent, especially south of the equator. The average water vapor mixing ratio in Fig. 15b over $\pm 24^\circ$ latitude is 3.3 ppmv. These patterns are similar to the climatological HALOE structures shown in Jackson et al. (1998) and Randel et al. (2001). The minima and average water vapor are lower during the La Niña cold event (Fig. 15b).

The difference map (Fig. 15c) indicates that during the warm event water vapor increases at 100 hPa in the

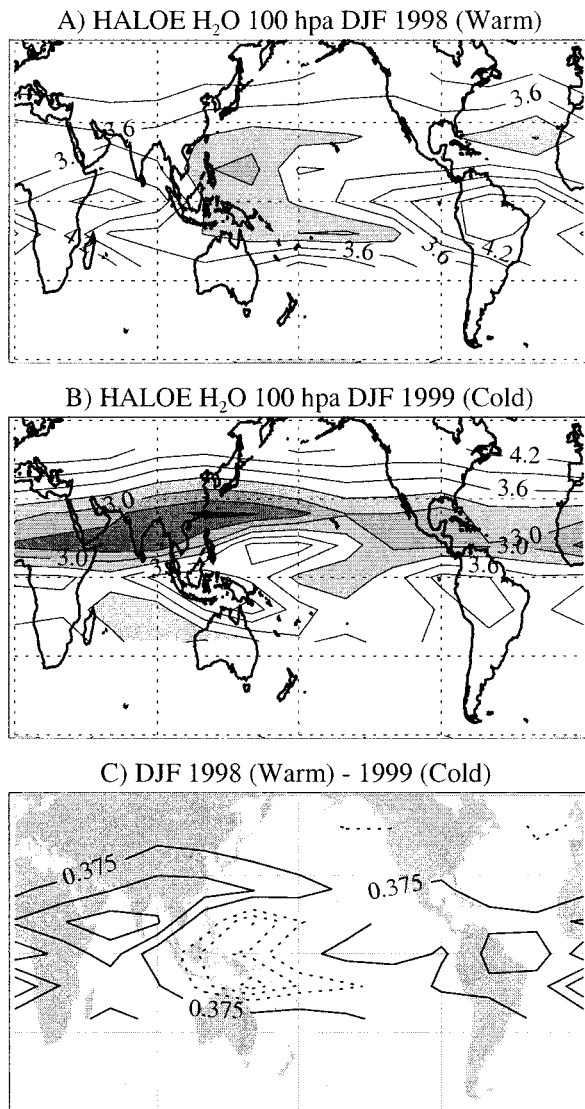


FIG. 15. DJF HALOE averaged water vapor mixing ratio at 100 hPa for (a) 1997–98 (ENSO warm) and (b) 1998–99 (ENSO cold). Contour interval of 0.3 ppmv. Levels less than 3.3 ppmv shaded. (c) Difference between these two seasons (contour interval 0.375 ppmv).

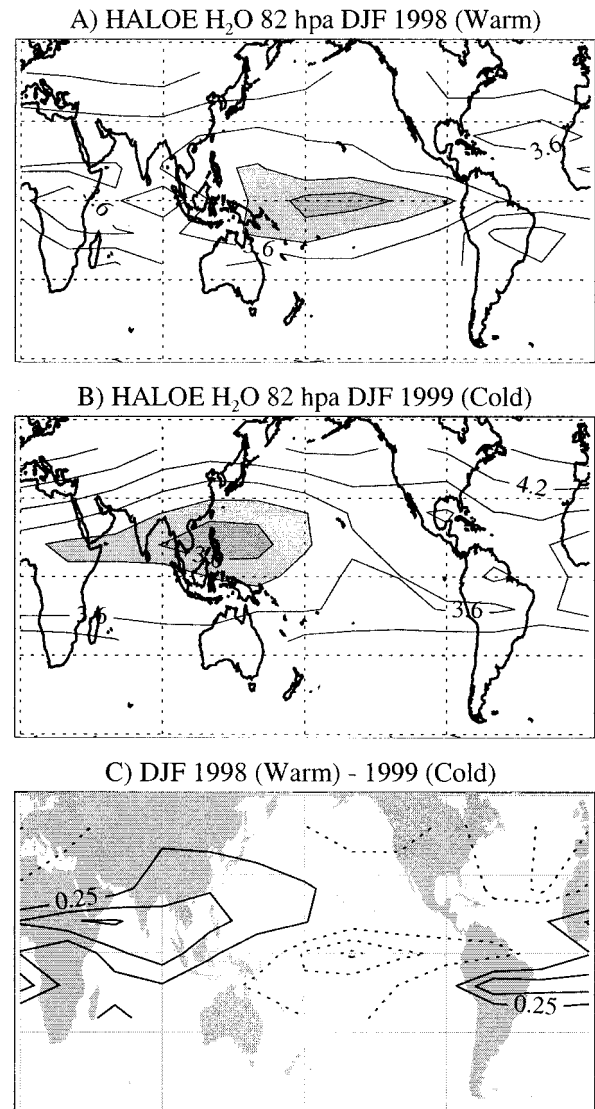


FIG. 16. DJF HALOE averaged water vapor mixing ratio at 82 hPa for (a) 1997–98 (ENSO warm) and (b) 1998–99 (ENSO cold). Contour interval of 0.3 ppmv. Levels less than 3.3 ppmv shaded. (c) Difference between these two seasons (contour interval 0.25 ppmv).

central and eastern Pacific and over the Indian Ocean, but decreases over the western Pacific. The pattern in the HALOE data at 100 hPa (Fig. 15) qualitatively resembles the difference maps at lower levels from MLS and the simulation (Figs. 13 and 14). At this level, it appears that water vapor is supplied to the tropopause region by convection directly below it, at least in the Pacific. The relationship is less clear over the Indian Ocean, but perhaps the water vapor is related to anomalies in convection (Fig. 2c) or the circulation (Fig. 5b) over Africa and the Indian Ocean.

A very different picture is evident in the HALOE water vapor data at 82 hPa (Fig. 16). This level is generally just above the thermal and cold point tropopause

throughout the Tropics. During the the 1997–98 ENSO warm event (Fig. 16a), the water vapor minimum (2.8 ppmv) is centered over the central and eastern Pacific at the equator. The tropical average of Fig. 16a is 3.7 ppmv. In contrast, during the 1998–99 ENSO cold event (Fig. 16b), water vapor has a broad minimum (also 2.8 ppmv) centered over the Philippines in the western Pacific (at about 15°N latitude). The tropical average of Fig. 16b is 3.6 ppmv. The difference map (Fig. 16c) indicates this shift in longitude and latitude, with lower water vapor over the central Pacific and higher water vapor over the western Pacific and Indian Ocean during the ENSO warm phase in 1998–99. Differences are up to 25% of the observed water vapor mixing ratios. Water

vapor does not appear to follow convection at this level, but rather water vapor is a minimum in the sectors where convection below (as measured by OLR) is a maximum, consistent with observations in the western Pacific by Vömel et al. (1995). The water vapor minimum also shifts from being on the equator during ENSO warm events to north of the equator during cold events. In both warm and cold events the water vapor minimum is observed well north of the regions of active convection (illustrated in Fig. 2). Jackson et al. (1998) have also noted that the seasonal minimum in water vapor as viewed from the HALOE instrument is north of the equator at 82 hPa during boreal winter (DJF). Similar qualitative patterns (though not as strong) occur at both 100 and 82 hPa if the analyses are performed on the periods analyzed in the MLS data (1995–96, 1996–97 for cold events and 1991–92, 1992–93 for warm events).

The model simulated water vapor fields in the tropopause region most closely corresponding to this region are at 99 hPa (Fig. 1). The water vapor distribution in the model is illustrated in Fig. 17 for the same seasons as Figs. 15 and 16. Water vapor in the CCM at this level appears not to resemble the CCM tropospheric patterns of Fig. 14 or the HALOE patterns at 100 hPa in Fig. 15. Instead, the patterns are strikingly similar to the distribution of HALOE water vapor at 82 hPa (Fig. 16). During the ENSO warm event in the simulation (Fig. 17a), the minimum in water vapor (2.5 ppmv) is centered over the equator, extending from the maritime continent to the coast of South America. The average water vapor concentration depicted in this panel averaged over $\pm 20^\circ$ latitude is 3.4 ppmv. During the cold event (Fig. 17b) the minimum in simulated water vapor (2.0 ppmv) is located just north of the equator in the western Pacific extending into the Indian Ocean, and a maximum south of the equator in the central and eastern Pacific. The average water vapor concentration depicted in this panel averaged over $\pm 20^\circ$ latitude is 3.2 ppmv. The difference plot between these seasons (Fig. 17c) looks similar to the difference plot of the HALOE data at 82 hPa (Fig. 16c), with slightly larger differences in the simulation, reaching 25% of the water vapor mixing ratio. An analysis of the monthly variation of averaged tropical water vapor in CCM3 at 99 hPa indicates a strong relationship (0.65 linear correlation of monthly mean anomalies) with the averaged 99-hPa temperature anomalies, which resemble the CCM3 tropopause temperature anomalies in Fig. 9 (dotted curve). Thus in the CCM3 simulation, water vapor at the cold point appears to be related to average tropopause temperature. Correlations with monthly minimum temperature or temperature at adjacent vertical levels above and below are not as strong.

Finally, we examine how ENSO affects the distribution of cirrus clouds in the tropopause region. Figure 18 presents seasonal averages of cirrus cloud extinction (in 10^{-3} km^{-1}) from HALOE for three levels: 82, 100, and 121 hPa during the 1998–99 ENSO cold event (Figs. 18a, 18c, and 18e) and the 1997–98 ENSO warm event

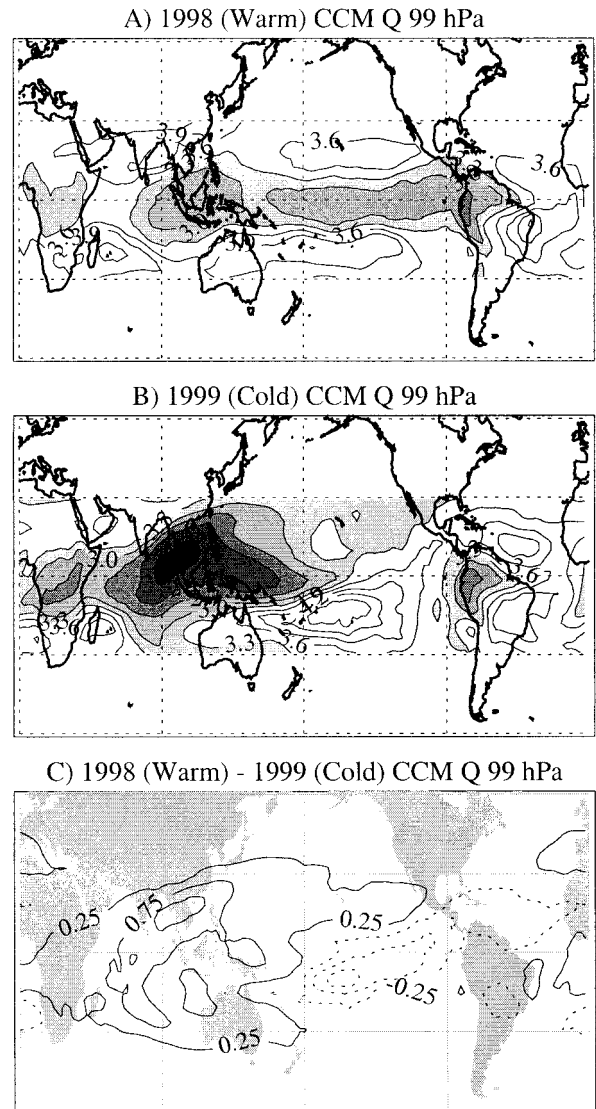


FIG. 17. Seasonal composites of CCM water vapor mixing ratio (Q) in parts per million by volume (ppmv) at 82 hPa for (a) 1998–99 and (c) 1997–98. Contour interval of 0.3 ppmv. Levels less than 3.3 ppmv shaded. Difference between these two seasons (contour interval 0.25 ppmv) is displayed in (c).

(Figs. 18b, 18d, and 18f). In both years, the average cirrus extinction decreases with decreasing pressure (increasing height). At all three levels, significant cirrus extinction appears over South America and Africa from the equator south. During the ENSO cold event (Figs. 18a, 18c, and 18e), high cirrus extinction is found over the western Pacific, Maritime Continent, and eastern Indian Ocean, while during the ENSO warm event (Figs. 18b, 18d, and 18f) this cirrus shifts (following the convection) into the central and eastern Pacific. Note that while the water vapor mixing ratio patterns are very different between the tropopause region (Fig. 16) and the upper troposphere (Fig. 13), the cirrus patterns are similar (Figs. 18a,b and 18e,f). Also note that the cirrus

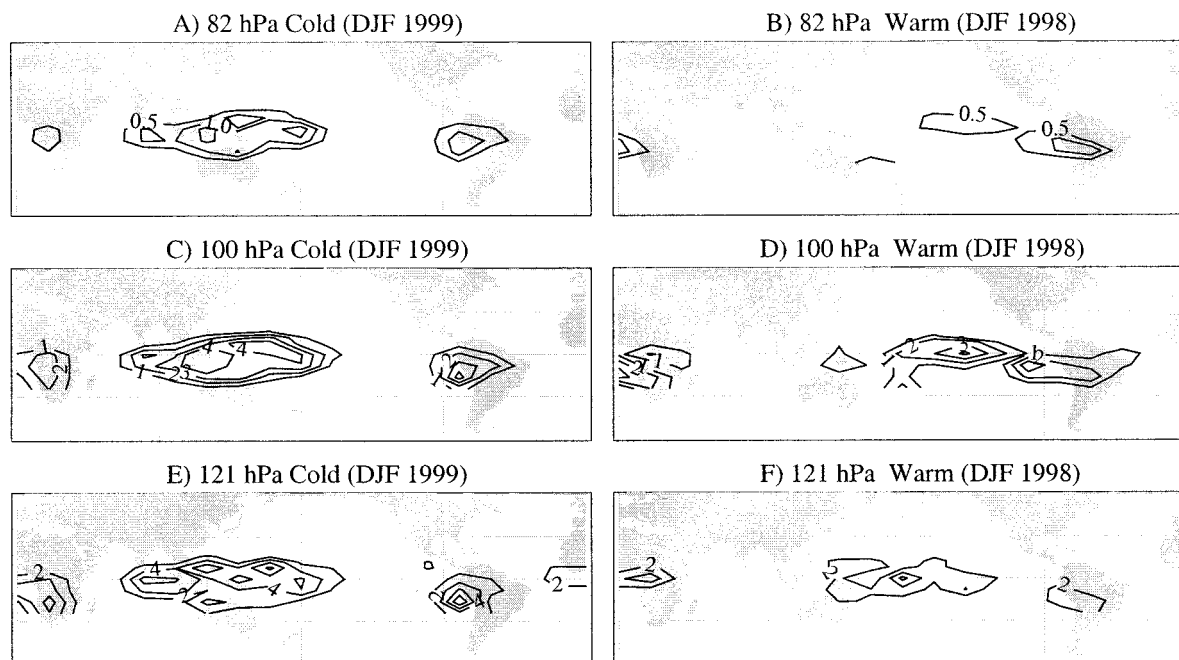


FIG. 18. Average DJF cirrus extinction from HALOE for (a), (c), and (e) 1998–99 and (b), (d), and (f) 1997–98. At three levels: (a) and (b) 82 hPa, (c) and (d) 100 hPa, and (e) and (f) 121 hPa. Extinction is measured in 10^{-3} km^{-1} . Contour intervals of (a) and (b) $2 \times 10^{-3} \text{ km}^{-1}$, (b) and (c) $1 \times 10^{-3} \text{ km}^{-1}$, and (e) and (f) $0.5 \times 10^{-3} \text{ km}^{-1}$.

extinction appears centered on the equator in all cases, and during the cold event extends barely to 15°N latitude.

Thus water vapor also responds strongly to the effects of ENSO. Water vapor in the upper troposphere is a maximum in the regions of convective activity, and water vapor in the tropopause region is a minimum in these same regions above convection. Cirrus clouds in the tropopause region remain near convection. The response of water vapor to ENSO in CCM3 resembles the observed response. In the model, water vapor variations appear linked to temperatures in the tropopause region.

7. Discussion

The variability associated with ENSO is a “natural experiment” with two different realizations of the upper tropical atmosphere, particularly in the tropical Pacific. There is a self-consistent relationship between tropical heating, the location of convection, changes in circulation patterns, and changes in tropical tropopause temperatures. These changes impact the water vapor distribution in the upper troposphere and the tropopause region.

ENSO is the dominant mode of variability for convection in the tropical Pacific (Fig. 3). The upper branch of the Walker circulation, centered at 150 hPa, is modulated by the changing location of convection due to ENSO (Fig. 5). These changes in convection and the circulation are associated with significant ENSO-related changes in the observed tropical tropopause temperature

(Fig. 10a) and potential temperature (Fig. 12). The tropopause changes are similar for thermal (lapse rate) and cold point tropopause definitions. A CCM3 forced by observed SSTs has similar OLR (Fig. 3b) and circulation (Fig. 6) responses. The changes due to ENSO can be well described by simple theories of tropical heat-induced circulations advanced by Gill (1980), when the redistribution of heat sources (chiefly latent heating from convection) as a result of ENSO (Fig. 8) are considered.

Despite the similarities between the model and observed responses, the interannual variations of tropical tropopause temperature, averaged over the Tropics, are vastly different (Fig. 9). Zonal mean anomalies in the model and observations are not correlated with ENSO. The observed tropopause temperature anomaly is due to the effects of processes not captured by the model, such as two major volcanic eruptions that occurred during this period (El Chichón in 1982 and Mount Pinatubo in 1991), the stratospheric QBO, or other “natural” variability, which is different between the atmosphere and this CCM3 simulation. All these processes may act to change atmospheric heating rates that drive the response of the tropopause region.

Analyses indicate that the thermal tropopause, particularly during a La Niña cold event, is not an isentropic surface (Fig. 11). Thus, parcels moving isentropically through a layer in the tropopause region may pass from tropospheric to stratospheric stability and back through a region of very cold temperatures. This has implica-

tions for water vapor, which may reach saturation in these cold areas. During ENSO warm events, tropopause θ decreases in the central Pacific, and thus tropopause θ is more zonally symmetric. The changes are consistent with results from Highwood and Hoskins (1998) that show that the large-scale dynamical response to tropospheric heating is a decrease in the potential temperature at the tropopause (above the heating). The decrease in tropopause θ can also be thought of as the result of local convective mass fluxes, which rapidly bring near-surface air into the upper troposphere. Convectively processed air in the upper troposphere has not experienced radiative heating and has a lower potential temperature than surrounding air (Folkins et al. 1999).

Water vapor at ~ 200 hPa in the upper troposphere is tightly coupled to convection in the observations (Fig. 13), based on changes during different phases of ENSO. CCM3 is able to reproduce these changes quite well (Fig. 14). At 100 hPa, HALOE observations indicate that water vapor behaves similar to the underlying layers (Fig. 15). At the level of the water vapor minimum (82 hPa in HALOE and 99 hPa in CCM3) the pattern is different. Water vapor is a minimum above convection, and extending around it. Cirrus clouds at all levels are found predominantly in the regions of active convection.

The water vapor minima at the cold point in both observations (Fig. 16) and the simulation (Fig. 17) extends well beyond the region of active convection and highlights the importance of horizontal transport in the tropopause region. The relationship between convection and water vapor above the tropopause is suggested by wind patterns at 150 hPa (Fig. 4), which move air from convective regions in the western Pacific northward. During ENSO warm events the modification to the circulation (Fig. 5) and convection (Fig. 3) in the central Pacific also changes the location of the water vapor minimum (Fig. 16).

The similarity of water vapor fields between the simulation (Fig. 17) and observations (Fig. 16), using a model with coarse spatial resolution and parameterized cloud processes, implies that the large-scale temperature structure and transport provide a good approximation for the water vapor distribution in the tropopause region. The simulation is able to represent ENSO variability in water vapor, forced by changes in convection and subsequent changes in tropopause region temperatures and circulations. Cirrus clouds processes or dehydration due to gravity wave temperature perturbations (neither of which are represented by the model), do not appear necessary to explain the distribution of water vapor (to first order). These smaller-scale processes may be important to explain details of the water vapor distribution.

Similar to observations, the average water vapor mixing ratio in the CCM3 simulation (3.2–3.4 ppmv) is significantly lower than the saturation mixing ratio of the average temperature (4.8–5.0 ppmv). This difference implies preferential regions of entry of air into the stratosphere where the air is cold. Newell and Gould-

Stewart (1981) hypothesized that this “Fountain” would occur in the western Pacific. But recent analyses by Sherwood (2000) and Gettelman et al. (2000) have indicated downward motion in the tropopause region in this area. An analysis of the vertical velocities from the CCM3 simulation indicates patterns of upward motion coincident with the location of convection up to 99 hPa. At 63 hPa however, particularly during la Niña episodes of convection concentrated over Indonesia, vertical velocities are downward above convection. This result should be treated with some caution, as the model does not resolve transport in the lower stratosphere. But it may in fact be that horizontal transport of air in the tropopause region is as important as vertical motion (convective or nonconvective) for determining the evolution of air and its chemical constituents in the tropopause region.

Acknowledgments. We thank L. Pan, F. Sassi, G. Branstator, R. Saravanan, and G. Kiladis and two anonymous reviewers for constructive comments on this paper. The National Center for Atmospheric Research (NCAR) is operated by the University Corporation for Atmospheric Research under the sponsorship of the National Science Foundation. A. Gettelman was supported at NCAR by the Advanced Study Program, the Atmospheric Chemistry Division, and the Climate and Global Dynamics Division.

REFERENCES

- Atticks, M. G., and G. D. Robinson, 1983: Some features of the structure of the tropical tropopause. *Quart. J. Roy. Meteor. Soc.*, **109**, 295–308.
- Bjerknes, J., 1969: Atmospheric teleconnections from the equatorial Pacific. *Mon. Wea. Rev.*, **97**, 163–172.
- Brewer, A. W., 1949: Evidence for a world circulation provided by the measurements of helium and water vapor distribution in the stratosphere. *Quart. J. Roy. Meteor. Soc.*, **75**, 351–363.
- Chandra, S., J. R. Ziemke, W. Min, and W. G. Read, 1998: Effects of 1997–1998 El Niño on tropospheric ozone and water vapor. *Geophys. Res. Lett.*, **25**, 3867–3870.
- de F. Forster, P. M., and K. P. Shine, 1999: Stratospheric water vapour changes as a possible contributor to observed stratospheric cooling. *Geophys. Res. Lett.*, **26**, 3309–3312.
- Deser, C., and J. M. Wallace, 1990: Large-scale atmospheric circulation features associated with warm and cold episodes in the tropical Pacific. *J. Climate*, **3**, 1254–1281.
- Folkins, I., M. Loewenstein, J. Podolske, S. J. Oltmans, and M. Profitt, 1999: A barrier to vertical mixing at 14 km in the Tropics: Evidence from ozonesondes and aircraft measurements. *J. Geophys. Res.*, **104** (D18), 22 095–22 102.
- Gage, K. S., and G. C. Reid, 1987: Longitudinal variations in tropical tropopause properties in relation to tropical convection and El Niño–Southern Oscillation events. *J. Geophys. Res.*, **92** (C13), 14 197–14 203.
- Gettelman, A., A. R. Douglass, and J. R. Holton, 2000: Simulations of water vapor in the upper troposphere and lower stratosphere. *J. Geophys. Res.*, **105**, 9003–9023.
- Gill, A. E., 1980: Some simple solutions for heat-induced tropical circulation. *Quart. J. Roy. Meteor. Soc.*, **106**, 447–462.
- Giorgetta, M. A., and L. Bengtsson, 1999: Potential role of the quasi-biennial oscillation in the stratosphere–troposphere exchange as

- found in water vapor in general circulation model experiments. *J. Geophys. Res.*, **104** (D6), 6003–6019.
- Harries, J. E., and Coauthors, 1996: Validation of measurements of water vapour from the Halogen Occultation Experiment (HALOE). *J. Geophys. Res.*, **101**, 10 205–10 216.
- Highwood, E. J., and B. J. Hoskins, 1998: The tropical tropopause. *Quart. J. Roy. Meteor. Soc.*, **124**, 1579–1604.
- Holton, J. R., P. H. Haynes, A. R. Douglass, R. B. Rood, and L. Pfister, 1995: Stratosphere–troposphere exchange. *Rev. Geophys.*, **33**, 403–439.
- Jackson, D. R., S. J. Driscoll, E. J. Highwood, J. E. Harries, and J. M. Russell III, 1998: Troposphere to stratosphere transport at low latitudes as studied using HALOE observations of water vapour 1992–1997. *Quart. J. Roy. Meteor. Soc.*, **124**, 169–192.
- Kalnay, E., and Coauthors, 1996: The NCEP/NCAR 40-Year Reanalysis Project. *Bull. Amer. Meteor. Soc.*, **77**, 437–471.
- Kiehl, J. T., J. J. Hack, G. B. Bonhan, B. A. Boville, B. P. Briegleb, D. L. Williamson, and P. J. Rasch, 1996: Description of the NCAR community climate model (CCM3). National Center for Atmospheric Research Tech. Rep. 420, 152 pp.
- Kiladis, G. N., K. H. Straub, G. C. Reid, and K. S. Gage, 2001: Aspects of interannual and intraseasonal variability of the tropopause and lower stratosphere. *Quart. J. Roy. Meteor. Soc.*, in press.
- Lorenz, E. N., 1956: Empirical orthogonal functions and statistical weather prediction. Dept. of Meteorology, Massachusetts Institute of Technology Tech. Rep. 1, 48 pp.
- Massie, S., P. Lowe, X. X. Tie, M. Hervig, G. Thomas, and J. M. Russell III, 2000: The effect of the 1997 El Niño on the distribution of upper tropospheric cirrus. *J. Geophys. Res.*, **105** (D18), 22 725–22 741.
- McCormack, J. P., R. Fu, and W. G. Read, 2000: The influence of convective outflow on water vapor mixing ratios in the tropical upper troposphere: An analysis based on UARS MLS measurements. *Geophys. Res. Lett.*, **27**, 525–528.
- Michelsen, H. A., F. W. Irion, G. L. Manney, G. C. Toon, and M. R. Gunson, 2000: Features and trends in ATMOS version 3 water vapor and methane measurements. *J. Geophys. Res.*, **105**, 22 713–22 724.
- Mote, P. W., and Coauthors, 1996: An atmospheric tape recorder: The imprint of tropical tropopause temperatures on stratospheric water vapor. *J. Geophys. Res.*, **101** (D2), 3989–4006.
- Newell, R. E., and S. Gould-Stewart, 1981: A stratospheric fountain? *J. Atmos. Sci.*, **38**, 2789–2796.
- , Y. Zhu, E. V. Browell, W. G. Read, and J. W. Waters, 1996: Walker circulation and tropical upper tropospheric water vapor. *J. Geophys. Res.*, **101** (D1), 1961–1974.
- Oltmans, S. J., H. Vömel, D. J. Hofmann, K. H. Rosenlof, and D. Kley, 2000: The increase in stratospheric water vapor from balloon-borne, frostpoint hygrometer measurements at Washington, D.C. and Boulder, Colorado. *Geophys. Res. Lett.*, **27**, 3453–3456.
- Oort, A. H., and J. J. Yienger, 1996: Observed interannual variability in the Hadley circulation and its connection to ENSO. *J. Climate*, **9**, 2751–2767.
- Philander, S. G., 1990: *El Niño, La Niña and the Southern Oscillation*. Academic Press, 293 pp.
- Randel, W. J., F. Wu, and D. J. Gaffen, 2000: Interannual variability of the tropical tropopause derived from radiosonde data and NCEP reanalyses. *J. Geophys. Res.*, **105** (D12), 15 509–15 523.
- , A. Gettelman, F. Wu, J. M. Russell III, J. Zawodny, and S. Oltmans, 2001: The seasonal variation of water vapour in the lowest stratosphere observed in HALOE data. *J. Geophys. Res.*, in press.
- Read, W. G., J. W. Waters, D. A. Flower, L. Froidevaux, R. F. Jarnot, D. L. Hartmann, R. S. Harwood, and R. B. Rood, 1995: Upper tropospheric water vapor from UARS MLS. *Bull. Amer. Meteor. Soc.*, **76**, 2381–2389.
- Reid, G. C., and K. S. Gage, 1981: On the annual variation in height of the tropical tropopause. *J. Atmos. Sci.*, **38**, 1928–1938.
- , and —, 1985: Interannual variations in the height of the tropical tropopause. *J. Geophys. Res.*, **90** (D3), 5629–5635.
- , and —, 1996: The tropical tropopause over the western Pacific: Wave driving, convection, and the annual cycle. *J. Geophys. Res.*, **101** (D16), 21 233–21 241.
- Russell, J. M., III, and Coauthors, 1993: The halogen occultation experiment. *J. Geophys. Res.*, **98** (D6), 10 777–10 797.
- Salby, M. L., and R. R. Garcia, 1987: Transient response to localized episodic heating in the Tropics. Part I: Excitation and short-time near-field behavior. *J. Atmos. Sci.*, **44**, 458–498.
- Sardeshmukh, P. D., and B. J. Hoskins, 1985: Vorticity balances in the Tropics during the 1982–83 El Niño–Southern Oscillation event. *Quart. J. Roy. Meteor. Soc.*, **111**, 261–278.
- , and —, 1988: The generation of global rotational flow by steady idealized tropical divergence. *J. Atmos. Sci.*, **45**, 1228–1251.
- Seidel, D. J., R. J. Ross, J. K. Angell, and G. C. Reid, 2001: Climatological characteristics of the tropical tropopause as revealed by radiosondes. *J. Geophys. Res.*, **106**, 7857–7878.
- Sherwood, S. C., 2000: A stratospheric “drain” over the Maritime Continent. *Geophys. Res. Lett.*, **27**, 677–680.
- Shindell, D. T., 2001: Climate and ozone response to increased stratosphere water vapor. *J. Geophys. Res. Lett.*, **28**, 1551–1554.
- SPARC, 2000: SPARC Assessment of water vapor in the upper troposphere and lower stratosphere. *Stratospheric Processes and Their Role in Climate*, WMO/TD-1043, 312 pp.
- Trenberth, K. E., and D. P. Stepaniak, 2001: Indices of El Niño evolution. *J. Climate*, **14**, 1697–1701.
- Vömel, H., S. Oltmans, D. Kley, and P. J. Crutzen, 1995: New evidence for the stratospheric dehydration mechanism in the equatorial Pacific. *Geophys. Res. Lett.*, **22**, 3235–3238.
- Walker, G. T., and E. W. Bliss, 1932: World weather V. *Mem. Roy. Meteor. Soc.*, **4**, 53–84.
- Webster, P. J., 1983: Large-scale structure of the tropical atmosphere. *Large-Scale Dynamical Processes in the Atmosphere*, B. Hoskins and R. Pearce, Eds., Academic Press, 235–275.
- , V. O. Magana, T. N. Palmer, J. Shukla, R. A. Thomas, M. Yanai, and T. Yasunari, 1998: Monsoons: Processes, predictability and the prospects for prediction. *J. Geophys. Res.*, **103** (C7), 14 451–14 510.
- Yulaeva, E., and J. M. Wallace, 1994: The signature of ENSO in global temperature and precipitation fields derived from the microwave sounding unit. *J. Climate*, **7**, 1719–1736.
- Zhou, X., M. A. Geller, and M. Zhang, 2001: Tropical cold point tropopause characteristics derived from ECMWF reanalyses and soundings. *J. Climate*, **14**, 1823–1838.